

3D-HST GRISM SPECTROSCOPY OF A GRAVITATIONALLY LENSED, LOW-METALLICITY STARBURST GALAXY AT $Z = 1.847^*$

GABRIEL B. BRAMMER¹, RUBÉN SÁNCHEZ-JANSSEN¹, IVO LABBÉ², ELISABETE DA CUNHA³, DAWN K. ERB⁴, MARIJN FRANX²,
MATTIA FUMAGALLI², BRITT LUNDGREN⁵, DANILO MARCHESINI⁶, IVELINA MOMCHEVA⁵, ERICA NELSON⁵, SHANNON PATEL²,
RYAN QUADRI⁷, HANS-WALTER RIX³, ROSALIND E. SKELTON⁵, KASPER B. SCHMIDT³, ARJEN VAN DER WEL³, PIETER G. VAN
DOKKUM⁵, DAVID A. WAKE⁵, KATHERINE E. WHITAKER⁵,

ApJL accepted (September 15, 2018)

ABSTRACT

We present *Hubble Space Telescope* (*HST*) imaging and spectroscopy of the gravitational lens SL2SJ02176-0513, a cusp arc at $z = 1.847$. The UV continuum of the lensed galaxy is very blue, which is seemingly at odds with its redder optical colors. The 3D-HST WFC3/G141 near-infrared spectrum of the lens reveals the source of this discrepancy to be extremely strong [O III] λ 5007 and H β emission lines with rest-frame equivalent widths of 2000 ± 100 and 520 ± 40 Å, respectively. The source has a stellar mass $\sim 10^8 M_{\odot}$, $sSFR \sim 100/\text{Gyr}$, and detection of [O III] λ 4363 yields a metallicity of $12 + \log(\text{O}/\text{H}) = 7.5 \pm 0.2$. We identify local blue compact dwarf analogs to SL2SJ02176-0513, which are among the most metal-poor galaxies in the SDSS. The local analogs resemble the lensed galaxy in many ways, including UV/optical SED, spatial morphology and emission line equivalent widths and ratios. Common to SL2SJ02176-0513 and its local counterparts is an upturn at mid-IR wavelengths likely arising from hot dust heated by starbursts. The emission lines of SL2SJ02176-0513 are spatially resolved owing to the combination of the lens and the high spatial resolution of *HST*. The lensed galaxy is composed of two clumps with combined size $r_e \sim 300$ pc, and we resolve significant differences in UV color and emission line equivalent width between them. Though it has characteristics occasionally attributed to active galactic nuclei, we conclude that SL2SJ02176-0513 is a low-metallicity star-bursting dwarf galaxy. Such galaxies will be found in significant numbers in the full 3D-HST grism survey.

Key words: galaxies: formation — galaxies: starburst — galaxies: dwarf — galaxies: high-redshift

1. INTRODUCTION

Tracing galaxy populations over cosmic time is key to understanding their evolutionary processes. Observations of a particular galaxy type over a range of redshifts yield complementary information, from spatially-resolved, high signal-to-noise studies of individual local examples to more distant statistical samples (e.g., Overzier et al. 2009). While local low-mass dwarfs ($\lesssim 10^9 M_{\odot}$) can be studied relatively easily, more distant examples are usually missing in typical flux-, mass-, or star-formation-rate-limited surveys. The best-studied examples at cosmological distances are usually strongly magnified by gravitational lenses (e.g., Fosbury et al. 2003; Yuan & Kewley 2009; Wuyts et al. 2012).

The lowest mass galaxies tend to have the lowest metallicities (Tremonti et al. 2004), and the normalization of this mass-metallicity relation evolves such that galaxies at a given

stellar mass have lower metallicities at higher redshifts to at least $z \sim 3$ (Erb et al. 2006; Mannucci et al. 2009). The physical conditions of low-metallicity star-forming galaxies can be very different than their higher-mass counterparts, characterized by a hard radiation field and strong stellar winds (e.g., Erb et al. 2010). Consequently they may have strong emission lines, which can be used to select them (Atek et al. 2011; van der Wel et al. 2011) and also must be accounted for when modeling their broad-band photometry (Atek et al. 2011; Finkelstein et al. 2011). Active galactic nuclei (AGN) are also sources of hard ionizing radiation that can result in similar spectral features, so accurately separating the influence of AGN and metallicity/star formation is crucial for understanding the dominant processes that shape galaxies at $z > 1$ (e.g., Trump et al. 2011).

In this Letter, we present *HST* observations of a gravitational lens system discovered by the Strong Lensing Legacy Survey consisting of a bright cusp arc at $z = 1.8470$ that is lensed by a massive galaxy at $z = 0.6459$ (SL2SJ02176-0513, Tu et al. 2009). The system lies within the CANDELS imaging (Grogin et al. 2011; Koekemoer et al. 2011) and 3D-HST spectroscopic (Brammer et al. 2012) surveys of the UKIDSS/UDS field. We use the unique combination of the *HST* datasets and the natural lens to demonstrate that the lensed galaxy is a low-mass, low-metallicity galaxy undergoing an extreme starburst, and that it shares many characteristics of local low-metallicity blue compact dwarf galaxies. We adopt cosmological parameters $h = 0.7$, $\Omega_m = 0.3$, and $\Omega_{\Lambda} = 0.7$ throughout.

2. OBSERVATIONS

We use the “v1.0” reduction of the 1–2 orbit *HST* ACS F606W, F814W and WFC3 F125W and F160W images pro-

gbrammer@eso.org

¹ European Southern Observatory, Alonso de Córdova 3107, Casilla 19001, Vitacura, Santiago, Chile

² Leiden Observatory, Leiden University, Leiden, The Netherlands

³ Max Planck Institute for Astronomy (MPIA), Königstuhl 17, 69117, Heidelberg, Germany

⁴ Department of Physics, University of Wisconsin-Milwaukee, P.O. Box 413, Milwaukee, WI 53201, USA

⁵ Department of Astronomy, Yale University, New Haven, CT 06520, USA

⁶ Physics and Astronomy Department, Tufts University, Robinson Hall, Room 257, Medford, MA, 02155, USA

⁷ Carnegie Observatories, 813 Santa Barbara Street, Pasadena, CA 91101, USA

* Based on observations made with the NASA/ESA *Hubble Space Telescope*, program #12328, obtained at the Space Telescope Science Institute, which is operated by the Association of Universities for Research in Astronomy, Inc., under NASA contract NAS 5-26555.

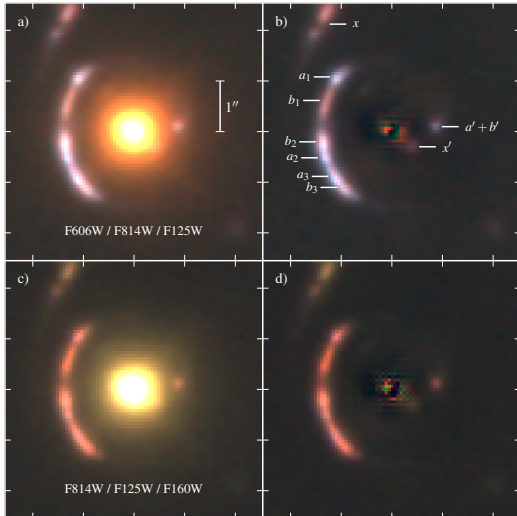


Figure 1. Three-color images of the UDS lens + arc system. Panels *a*) and *b*) are made from ACS F606W (blue), F814W (green) and WFC3 F125W (red). Panels *c*) and *d*) are made from ACS F814W (blue), WFC3 F125W (green), and F160W (red). All images are PSF-matched to F160W. The band-dependent `galfit` model of the foreground lens galaxy is subtracted from the right panels. The object lensed into the cusp arc is composed of two primary clumps, “*a*” and “*b*,” and the conjugate image positions are shown in panel *b*). The conjugate images of an additional lensed object (Tu et al. 2009; Cooray et al. 2011) are labeled “*x*.”

vided by the CANDELS team (Koekemoer et al. 2011). Three-color combinations of the CANDELS images are shown in Figure 1. The arc is very blue through the observed optical and F125W bands, with the UV slope $\beta = -1.7 \pm 0.2$ ($f_\lambda \propto \lambda^\beta$) determined from the two ACS bands ($\lambda_{\text{rest}} = 2100\text{--}2800\text{\AA}$). The arc becomes surprisingly red when the F160W band is included; Cooray et al. (2011) hypothesized that the red F125W–F160W color is caused by strong [O III] emission that dominates the flux in the redder band, similar to the extreme equivalent-width galaxies discovered by van der Wel et al. (2011). In addition to the *HST* observations, we extract photometry of the arc from CFHT-LS *ugriz* and UKIDSS/UDS *JHK* imaging following Cooray et al. (2011) and removing the roughly symmetric lens galaxy by subtracting a flipped version of the ground-based images.

SL2SJ02176-0513 was observed with the WFC3 G141 grism on 2011 December 21 as part of the 3D-HST survey. The spectrum was reduced as described in detail by Brammer et al. (2012). Figure 2 shows the remarkable G141 spectrum of the lens system, with strong emission lines of [O III] λ 4959+5007, H β , and H γ (potentially blended with [O III] λ 4363) that explain the colors in Figure 1 and confirm the prediction of Cooray et al. (2011). All of the emission lines are extended, showing the same morphology as the UV (ACS) continuum. The emission lines prove that the arc and counter image lie at the same redshift.

The SL2SJ02176-0513 system is a bright MIPS $24\mu\text{m}$ source⁹ with a total flux of 0.565 mJy, offset from the lens galaxy and centered on the arc. From a simultaneous fit (see Labbé et al. 2006) of the $24\mu\text{m}$ contributions from the arc, the lens, and the additional $z = 2.3$ lensed galaxy to the north, we find that the arc contributes 85% of the $24\mu\text{m}$ flux, or 0.476 ± 0.025 mJy.

3. ANALYSIS

⁹ <http://irsa.ipac.caltech.edu/data/SPITZER/SpUDS>

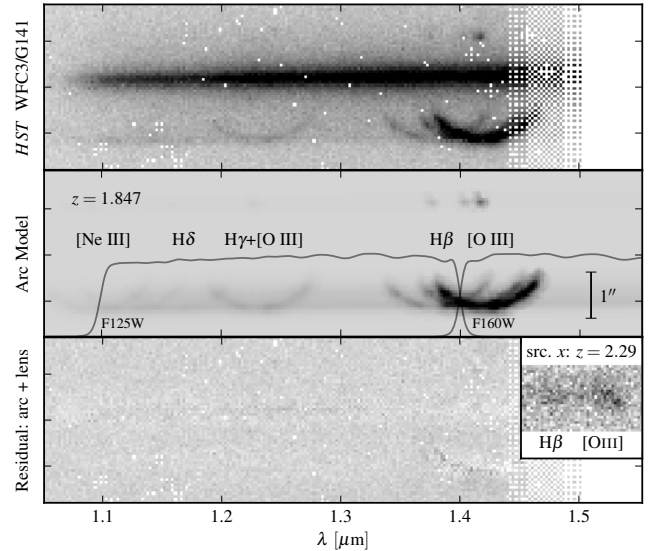


Figure 2. Two-dimensional slitless WFC3/G141 spectrum of the UDS lens + arc system from 3D-HST. **Top:** The combined spectrum of the $z = 0.656$ lens galaxy and the arc. The dispersion axis lies roughly along the arc resulting in a clean separation of the arc and lens but also in overlapping emission lines. **Middle:** The modeled line+continuum two-dimensional spectrum. The G141 spectrum is cut off at the edge of the 3D-HST pointing; the pixelated structure at $\sim 1.45\mu\text{m}$ is the result of the dither pattern. **Bottom:** Residuals of the lens + arc model fit. The small inset panel shows detections from an adjacent 3D-HST pointing of weak H β and [O III] emission lines for the lensed source “*x*” (Figure 1) at $z = 2.29$.

3.1. Lens magnification

Below we determine physical properties of SL2SJ02176-0513 integrated over the full arc, which is composed of three magnified images of the source (Figure 1). To estimate an upper limit on the true physical scales of the source, we consider the brightness and size of the faint counter image opposite of the arc. We determine a brightness ratio $\mu_* = 25$ between the integrated arc and the counter image. The magnification of the counter image, μ' , is ~ 1.4 given the lens model parameters of Cooray et al. (2011). The counter image, which includes both clumps resolved in the arc, has $\sqrt{\mu'} \cdot r_e = 1.4 \text{ pix} = 0''.04 = 350 \text{ pc}$, $r_e \sim 300 \text{ pc}$ in the ACS images.

3.2. Modeling the grism spectrum

In order to extract quantities from the grism spectrum, we generate and fit a model of the two-dimensional spectrum that essentially convolves an arbitrary one-dimensional spectrum with an assumed object morphology, given the grism dispersion configuration files provided by STScI. To model the contribution of the lens to the flux at the location of the arc, we adopt as the lens morphology an analytical Sersic profile with parameters determined by running `galfit` (Peng et al. 2002) on the 3D-HST F140W image. For the arc, we adopt the observed (lens-subtracted) F140W morphology and a one-dimensional spectrum that consists of a $Z = 0.008$ Bruzual & Charlot (2003) single stellar population model for the continuum and individual emission lines.

The model is fit to the observed spectrum with parameters optimized by the `emcee` Markov Chain Monte-Carlo sampler (Foreman-Mackey et al. 2012), where the free parameters are 1) a spatial shift and a spectral scaling to improve the subtraction of the lens, 2) the redshift of the arc, 3) the age, stellar mass, and reddening of the arc continuum following a Calzetti

Table 1
Observables and derived quantities

Parameter	Value
R.A., Dec.	02:17:37.237, -05:13:29.78
<i>Photometry</i>	
F606W (V) [AB]	22.07 ± 0.03
F814W (i)	21.96 ± 0.03
F125W (J)	21.71 ± 0.02
F140W (H_{wide})	21.10 ± 0.04
F160W (H)	20.90 ± 0.02
MIPS 24 μm [mJy]	0.476 ± 0.025
μ_*	25 ± 1^a
μ'	$\sim 1.4^a$
<i>Spectrum + SED fit</i>	
z	$1.84691 \pm 0.0004^{\text{rand}} \pm 0.002^{\text{sys}}$
$\log(\text{age/yr})$	7.2 ± 0.2
A_V (continuum)	0.09 ± 0.15
$\log(\mu \cdot M/M_\odot)$	9.5 ± 0.1
$f([\text{O III}]\lambda\lambda 4959+5007)$	309 ± 2^b
$f(\text{H}\beta)$	74 ± 2^b
$f(\text{H}\gamma + [\text{O III}]\lambda 4363)$	40 ± 3^b
$f(\text{H}\delta)$	13 ± 2^b
$f(\text{Ne III}\lambda 3869)$	30 ± 4^b
$EW_{\text{O III}}$	$5690 \pm 290 \text{ \AA}^c$
$EW_{\text{H}\beta}$	$1470 \pm 110 \text{ \AA}^c$
<i>Derived parameters</i>	
β (2000–2800 \AA)	-1.7 ± 0.2
$\mu \cdot \text{SFR}_{\text{H}\beta}$ ($M_\odot \text{ yr}^{-1}$)	390 ± 9
$12 + \log(\text{O}/\text{H})$	7.5 ± 0.2
$\sqrt{\mu' \cdot r_e}$	350 pc
$\Sigma_{\text{SFR}} (r < r_e, M_\odot \text{ yr}^{-1} \text{ kpc}^{-2})$	20

^a μ_* is the relative magnification between the integrated arc and the counter image. μ' is the brightness magnification of the counter image. The total lens magnification is $\mu = \mu_* \cdot \mu'$.

^b Line fluxes are in $10^{-17} \text{ erg s}^{-1} \text{ cm}^{-2}$, uncorrected for lens magnification.

^c Observed frame

et al. (2000) reddening law, and 4) individual strengths of the arc emission lines $[\text{O III}]\lambda 4959+5007$, $\text{H}\beta$, $\text{H}\gamma$, $[\text{O III}]\lambda 4363$, $\text{H}\delta$, $\text{H}\epsilon$, and $\text{Ne III}\lambda 3869$. While the spectral resolution of the G141 grism ($R \sim 130$) is insufficient to resolve the $\text{H}\gamma$ and $[\text{O III}]\lambda 4363$ lines, the *sum* of these lines is well-constrained by the G141 spectrum.

The best-fit model of the 2D arc spectrum is shown in the middle panel of Figure 2, and the residuals of the full lens+arc model fit are shown in the bottom panel. The parameters of the model, including the line strengths and observed-frame equivalent widths are summarized in Table 1. The uncertainties on all parameters come from the full marginalized posterior distribution function of the MCMC chain. The most robust fits are for the $\lambda 4959+5007$ and $\text{H}\beta$ emission line strengths, with rest-frame equivalent widths of 2000 ± 100 and $520 \pm 40 \text{ \AA}$, respectively. We obtain a marginal detection of $[\text{O III}]\lambda 4363$ at $5 \pm 3 \times 10^{-17} \text{ erg s}^{-1} \text{ cm}^{-2}$ assuming an intrinsic Balmer line ratio $\text{H}\gamma/\text{H}\beta = 0.468$ and no reddening of the Balmer lines. The $[\text{O III}]\lambda 4363$ flux will be higher for any non-zero Balmer decrement.

3.3. Fundamental quantities: star-formation rate, stellar mass, and metallicity

The luminosity of the $\text{H}\beta$ line corresponds to a de-magnified star-formation rate of $11 M_\odot \text{ yr}^{-1}$ ($\text{H}\alpha/\text{H}\beta = 2.86$ Dopita & Sutherland 2003; Kennicutt 1998). The $\text{H}\gamma/\text{H}\beta$ ratio is consistent with $E(B-V) = 0$. The de-magnified stellar mass determined from the combined fit to the UV+optical

SED and G141 spectrum is $9 \times 10^7 M_\odot$, similar to the average stellar mass of the equivalent-width-selected galaxies from van der Wel et al. (2011). The specific star-formation rate of SL2SJ02176-0513 is extremely high (as expected given the extreme line equivalent widths), with a mass doubling time of only 9 Myr ($s\text{SFR} \sim 100 \text{ Gyr}^{-1}$).

The (implied) detection of the $[\text{O III}]\lambda 4363$ line suggests that SL2SJ02176-0513 has a low metallicity as that line can only form in hot H II regions with little metal-line cooling. To estimate the metallicity, we draw values of the line fluxes and A_V from the full marginalized PDF of the MCMC fit. Assuming that the continuum A_V also attenuates the Balmer lines, a given A_V determines the relative fluxes of $\text{H}\gamma$ and $[\text{O III}]\lambda 4363$ given the observed $\text{H}\beta$ flux and a Balmer decrement. Combining the observed lines with a random uniform distribution $[\text{O III}]\lambda 5007/[\text{O II}]\lambda 3727 = [2.5, 9]$ (Erb et al. 2010; Atek et al. 2011), we use the prescription of Izotov et al. (2006) and determine $T(\text{O III}) = 17000 \pm 3000 \text{ K}$ and $12 + \log(\text{O}/\text{H}) = 7.5$, or $\sim 6\%$ of the solar value ($12 + \log(\text{O}/\text{H}) = 8.69$, Asplund et al. 2009). The posterior probability on $12 + \log(\text{O}/\text{H})$ has (16, 84) percentiles of (7.3, 7.7), but with an extended tail towards higher metallicities ($P = 5\%$ for $12 + \log(\text{O}/\text{H}) > 8$) given the low significance of the $[\text{O III}]\lambda 4363$ detection.

4. LOCAL ANALOGS: LOW-METALLICITY BLUE COMPACT DWARF GALAXIES

While the unique observational data of SL2SJ02176-0513 paint a self-consistent picture of an extremely low-metallicity, low-mass starburst galaxy, many of the simplifying assumptions underlying its derived properties can result in significant systematic uncertainties. To place the properties of SL2SJ02176-0513 in context with nearby galaxies, we select a comparison sample from the Sloan Digital Sky Survey (SDSS DR7, Abazajian et al. 2009) with $EW_{\text{O III}} > 1500 \text{ \AA}$ and $\log(f_{\text{O III}}/f_{\text{H}\beta}) < 0.75^{10}$ as measured by Brinchmann et al. (2004).

This simple selection criterion reduces the full SDSS spectroscopic sample of 930 000 galaxies to just 14. Of these, eight objects have $12 + \log(\text{O}/\text{H}) > 8$ (within the fiber aperture, Tremonti et al. 2004) and are in fact compact, especially blue, individual H II regions in spiral/irregular galaxies (M101 and M106 among them). The remaining six objects are blue compact dwarf galaxies with $12 + \log(\text{O}/\text{H}) < 8$. Four are found in the extremely metal-poor galaxy compilation by Morales-Luis et al. (2011) with $12 + \log(\text{O}/\text{H}) \sim 7.6$ and the final two have $12 + \log(\text{O}/\text{H}) \sim 7.8$ (Brinchmann et al. 2008; Engelbracht et al. 2008).

4.1. Spectral energy distributions

Three of these local analog galaxies are compared to SL2SJ02176-0513 in Figure 3. The left panel demonstrates the similarity of the SEDs of SL2SJ02176-0513 and its local analogs at all observed wavelengths: all have similar blue UV continua, and the optical/NIR photometry of the analogs agrees well with the extrapolation of the lens stellar continuum fit. SL2SJ02176-0513 is 2–20 times more luminous than the local analogs shown, qualitatively consistent with the order of magnitude increase of stellar mass at constant metallicity to $z \sim 2$ (e.g., Erb et al. 2006). Both samples show

¹⁰ $[\text{O III}] \equiv [\text{O III}]\lambda 4959 + [\text{O III}]\lambda 5007$

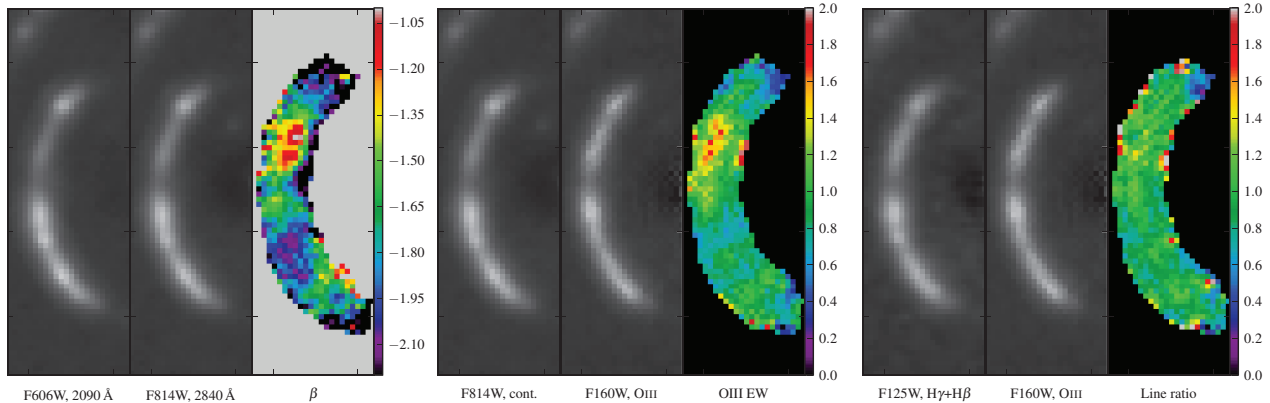


Figure 4. Ratios of aligned ACS and WFC3 images. The `galfit` model of the foreground lens has been subtracted from all images and the residual images in the different bands are PSF-matched to the F160W PSF. **Left:** Ratio of the ACS F606W and F814W images, combined to provide a map of the UV slope, β , where $F_\lambda \propto \lambda^\beta$. **Center:** Ratio of the WFC3 F160W image, which is dominated by the [O III] emission lines, to F814W, which is taken to represent the continuum. The result is a map of the emission line equivalent width across the arc. **Right:** The ratio of WFC3 F160W and F125W roughly indicates spatial variations in the [O III] to Balmer emission line ratio across the arc. The line ratio is much more uniform than the line equivalent widths.

F160W (line) and F814W (continuum) images, however, the F160W ([O III]) to F125W (Balmer line) ratio is roughly constant across the arc. The differences between the sources is most apparent for the a_1 and b_1 components that are best separated by the lens, though the other pairs of conjugate images show roughly the same trends. The individual super star clusters in SBS 0335-052E show differences in broad-band colors and line ratios comparable to those in Figure 4 (Thuan et al. 1997; Izotov et al. 2009).

5. DISCUSSION AND SUMMARY

We take advantage of the unique combination of a natural gravitational lens and high spatial resolution *HST* imaging and near-IR spectroscopy to extract the detailed properties of SL2SJ02176-0513. The near-IR spectrum is dominated by extremely strong emission lines of $H\gamma$, $H\beta$ and [O III] at $z = 1.847$. From the UV/optical spectrum and photometry, we determine that the source of SL2SJ02176-0513 is a young starbursting ($sSFR \sim 100/\text{Gyr}$) dwarf galaxy ($M \sim 1.3 \times 10^8 M_\odot$) with an extremely low gas-phase metallicity ($12 + \log(\text{O}/\text{H}) \sim 7.5$). Even with so few metals, SL2SJ02176-0513 shows detectable hot dust emission observed at $\lambda_{\text{obs}} = 24 \mu\text{m}$.

We find the unique properties of SL2SJ02176-0513 to be remarkably similar to those of nearby low-metallicity blue compact dwarf galaxies selected to have similar [O III] equivalent widths and ([O III]/ $H\beta$) line ratios. Such galaxies are frequently considered to be local analogs to galaxies expected to be more common at earlier cosmic times and in SL2SJ02176-0513 we have discovered a compelling connection at high redshift (which itself is likely a bright, magnified example of the galaxies discovered by van der Wel et al. 2011).

SL2SJ02176-0513 has characteristics that are frequently attributed to AGN at similar redshifts: extreme equivalent widths and line ratios of the optical emission lines, high-ionization UV lines, and the presence of a strong IR excess from heated dust. We demonstrate that all of these properties are largely consistent with a hard ionization field produced by a compact, low metallicity starburst (see also examples from Fosbury et al. 2003; Erb et al. 2010 and discussion by Hunt et al. 2010). Further evidence comes from the fact that the lens resolves two line-emitting components of SL2SJ02176-0513, though extended narrow-line regions excited by nuclear activity have been observed (e.g., Unger et al. 1987). Both star-

formation and AGN reach a peak in their activity at $z \sim 2$ so robust identification and separation of the two contributions is critical for understanding their effect on galaxy evolution.

We conclude by noting that we will obtain a substantial sample of (unlensed) galaxies with similar, if not quite as extreme, properties to SL2SJ02176-0513 at $1.3 < z < 2.2$ (covering [O III]+ $H\beta$) in the full 3D-HST survey. Without the factor of ~ 25 lens magnification, such an object would have $m_{\text{F140W}} = 25.2$, where 3D-HST is sensitive to line equivalent widths $\gtrsim 1000 \text{ \AA}$ (Brammer et al. 2012). Indeed many such galaxies have recently been found with WFC3 (Atek et al. 2011; van der Wel et al. 2011). While individual unlensed objects will not allow such detailed study as performed here, statistical samples of these galaxies will offer insights into the metallicity and star-formation properties of the low-mass building blocks of galaxies observed today.

We thank the referee, M. Malkan, for constructive comments that greatly improved the manuscript and R. Gavazzi and T. Treu for helpful discussions and for providing the LRIS spectrum of SL2SJ02176-0513. This publication makes use of data products from the Wide-field Infrared Survey Explorer, which is a joint project of the University of California, Los Angeles, and the Jet Propulsion Laboratory/California Institute of Technology, funded by the National Aeronautics and Space Administration. Funding for this research was provided in part by the Marie Curie Actions of the European Commission (FP7-COFUND) and ERC grant HIGHZ no. 227749.

Facilities: Hubble Space Telescope (WFC3)

REFERENCES

- Abazajian, K. N., Adelman-McCarthy, J. K., Agüeros, M. A., et al. 2009, *ApJS*, 182, 543
 Asplund, M., Grevesse, N., Sauval, A. J., et al. 2009, *ARA&A*, 47, 481
 Atek, H., Siana, B., Scarlata, C., et al. 2011, *ApJ*, 743, 121
 Brammer, G. B., van Dokkum, P. G., Franx, M., et al. 2012, *ApJS*, 200, 13
 Brinchmann, J., Charlot, S., White, S. D. M., et al. 2004, *MNRAS*, 351, 1151
 Brinchmann, J., Kunth, D., & Durret, F. 2008, *A&A*, 485, 657
 Bruzual, G., & Charlot, S. 2003, *MNRAS*, 344, 1000
 Calzetti, D., Armus, L., Bohlin, R. C., et al. 2000, *ApJ*, 533, 682
 Cooray, A., Fu, H., Calanog, J., et al. 2011, *ArXiv e-prints*
 Dopita, M. A., & Sutherland, R. S. 2003, *Astrophysics of the diffuse universe*

- Engelbracht, C. W., Rieke, G. H., Gordon, K. D., et al. 2008, *ApJ*, 678, 804
- Erb, D. K., Pettini, M., Shapley, A. E., et al. 2010, *ApJ*, 719, 1168
- Erb, D. K., Steidel, C. C., Shapley, A. E., et al. 2006, *ApJ*, 646, 107
- Finkelstein, S. L., Papovich, C., Salmon, B., et al. 2011, *ArXiv e-prints*
- Foreman-Mackey, D., Hogg, D. W., Lang, D., et al. 2012, *ArXiv e-prints*
- Fosbury, R. A. E., Villar-Martín, M., Humphrey, A., et al. 2003, *ApJ*, 596, 797
- Griffith, R. L., Tsai, C.-W., Stern, D., et al. 2011, *ApJ*, 736, L22
- Grogin, N. A., Kocevski, D. D., Faber, S. M., et al. 2011, *ApJS*, 197, 35
- Hainline, K. N., Shapley, A. E., Greene, J. E., et al. 2011, *ApJ*, 733, 31
- Hirashita, H., & Hunt, L. K. 2004, *A&A*, 421, 555
- Hunt, L. K., Thuan, T. X., Izotov, Y. I., et al. 2010, *ApJ*, 712, 164
- Izotov, Y. I., Guseva, N. G., Fricke, K. J., et al. 2011, *A&A*, 536, L7
- , 2009, *A&A*, 503, 61
- Izotov, Y. I., Lipovetsky, V. A., Chaffee, F. H., et al. 1997, *ApJ*, 476, 698
- Izotov, Y. I., Stasińska, G., Meynet, G., et al. 2006, *A&A*, 448, 955
- Kennicutt, Jr., R. C. 1998, *ARA&A*, 36, 189
- Koekemoer, A. M., Faber, S. M., Ferguson, H. C., et al. 2011, *ApJS*, 197, 36
- Labbé, I., Bouwens, R., Illingworth, G. D., et al. 2006, *ApJ*, 649, L67
- Malkan, M. A., Teplitz, H., & McLean, I. S. 1996, *ApJ*, 468, L9
- Mannucci, F., Cresci, G., Maiolino, R., et al. 2009, *MNRAS*, 398, 1915
- Morales-Luis, A. B., Sánchez Almeida, J., Aguerri, J. A. L., et al. 2011, *ApJ*, 743, 77
- Overzier, R. A., Heckman, T. M., Tremonti, C., et al. 2009, *ApJ*, 706, 203
- Peng, C. Y., Ho, L. C., Impey, C. D., et al. 2002, *AJ*, 124, 266
- Reines, A. E., Johnson, K. E., & Hunt, L. K. 2008, *AJ*, 136, 1415
- Thuan, T. X., Izotov, Y. I., & Lipovetsky, V. A. 1997, *ApJ*, 477, 661
- Thuan, T. X., Sauvage, M., & Madden, S. 1999, *ApJ*, 516, 783
- Todini, P., & Ferrara, A. 2001, *MNRAS*, 325, 726
- Tremonti, C. A., Heckman, T. M., Kauffmann, G., et al. 2004, *ApJ*, 613, 898
- Trump, J. R., Weiner, B. J., Scarlata, C., et al. 2011, *ApJ*, 743, 144
- Tu, H., Gavazzi, R., Limousin, M., et al. 2009, *A&A*, 501, 475
- Unger, S. W., Pedlar, A., Axon, D. J., et al. 1987, *MNRAS*, 228, 671
- van der Wel, A., Straughn, A. N., Rix, H.-W., et al. 2011, *ApJ*, 742, 111
- Wright, E. L., Eisenhardt, P. R. M., Mainzer, A. K., et al. 2010, *AJ*, 140, 1868
- Wuyts, E., Rigby, J. R., Sharon, K., et al. 2012, *ArXiv e-prints*
- Yuan, T.-T., & Kewley, L. J. 2009, *ApJ*, 699, L161